communications physics

Article

https://doi.org/10.1038/s42005-024-01601-0

Intensity-tunable achromatic cascade liquid crystal Pancharatnam-Berry lens

Zhichang Mo[1,2,3], Yuanan Zhao[1,2,3] ✉, Jianguo Wang[1,2,3], Xiaofeng Liu[1,2,3], Changjie Cheng[4], Yi Chen[1], Xiangyu Zhu[1], Yadi Zhao[1,2,3], Kun Wang[1,5], Shaozhong Ou[1,5], Zhouhao Zhang[1,6], Zhaoliang Cao[7], Qing Cao[4] ✉ & Jianda Shao[1,2,3,8] ✉

In the current solution for multiwavelength achromatic flat lenses, a one-to-one correspondence exists between the number of writing phase distributions and the number of achromatic wavelengths. Breaking this correspondence requires a complex phase design and parameter optimization. Here, we show that a dual-layer cascade liquid crystal Pancharatnam-Berry lens (CLCPBL) with two writing phase distributions and a specific coupled phase distribution between the layers can achieve three wavelength achromaticity without any parameter optimization process. Similarly, in a three-layer cascade, the number of achromatic wavelengths increases to seven through the permutations of the layers, with adjustable amplitude factors. We fabricate a three-layer CLCPBL with the design wavelengths of 396.8 nm, 1064 nm, and 1550 nm, which theoretically allows the light at 632.8, 532.8, 3383 and 450 nm to form a common focus, and test such structure. Our CLCPBL enables a wider range of applications than conventional achromatic flat lenses.

Researchers have found that the chromatic aberration[1–3], stemming from dispersion, can disrupt numerous imaging systems. This necessitates the utilization of components such as achromatic lenses to achieve wide-spectrum or multiwavelength dispersion compensation, facilitating the acquisition of precise, lucid, and distinct imaging patterns. A typical achromatic lens assembly comprises two or more cascaded lenses. With meticulous design and optimization of the lens structure and materials[4], the co-focusing of two or more wavelengths can be achieved by employing the appropriate number of lenses. Advancements in binary optics[5] have led to the development of components such as Fresnel lenses and photon sieves[6,7], which employ the principle of diffraction and exhibit negative dispersion characteristics. This has led to the proposal of hybrid refraction-diffraction achromatic systems[8–10], for example, a catadioptric pancake lens was formed by a planar and broadband cholesteric liquid crystal lens hybridized with a refractive lens[11]. This structure has high image quality and excellent achromatic performance in the display spectral range, which is expected to be applied to catadioptric VR display systems.

In response to the pressing demand for lightweight and compact optical systems, the concept of metasurfaces[12,13] was proposed. By incorporating subwavelength metal antennas or highly refractive dielectric units in a thin film, flexible manipulation of the amplitude, phase, and other parameters of light can be achieved. Comprehensive designs and fabrication processes have been established for diverse devices and applications such as metalenses[14], optical switches[15], holograms[16,17], and optical codings[18]. Metalenses have excellent potential for application in microscopic imaging[19], photolithography[20], Augmented reality/Virtual reality (AR/VR)[21,22], and other domains. However, regardless of whether the phase modulation in these elements arises from the propagation phase[23], detour phase[24], or Pancharatnam-Berry (PB) phase[25,26], they still exhibit the inherent negative dispersion characteristics of diffractive lenses. Consequently, they can only fulfill the focusing requirements for a single wavelength and fail to address scenarios requiring broadband or multiwavelength capabilities. Recent investigations of achromatic

[1]Laboratory of Thin Film Optics, Shanghai Institute of Optics and Fine Mechanics, Shanghai 201800, China. [2]Center of Materials Science and Optoelectronics Engineering, University of Chinese Academy of Sciences, 100049 Beijing, China. [3]Key Laboratory of Materials for High Power Laser, Chinese Academy of Sciences, Shanghai 201800, China. [4]College of Sciences, Department of Physics, Shanghai University, Shanghai 201800, China. [5]School of Optical-Electrical and Computer Engineering, University of Shanghai for Science and Technology, Shanghai 200093, China. [6]Henan Key Laboratory of Infrared Materials & Spectrum Measures and Applications, School of Physics, Henan Normal University, Xinxiang 453007, China. [7]Jiangsu Key Laboratory of Micro and Nano Heat Fluid Flow Technology and Energy Application, School of Physical Science and Technology, Suzhou University of Science and Technology, Suzhou 215009, China. [8]Hangzhou Institute for Advanced Study, University of Chinese Academy of Sciences, Hangzhou 310024, China. ✉e-mail: yazhao@siom.ac.cn; qcao@shu.edu.cn; jdshao@siom.ac.cn

metalenses have offered new solutions. For instance, precise control of the parameters of coupled rectangular dielectric resonators, which serve as the building blocks of metalenses, enables confocal performance at wavelengths of 1300, 1550, and 1800 nm[27]. In addition, the design of spatial multiplexing structures[28] or multi-layer stacking configurations[29] can achieve achromatic functions for multiwavelength applications. Furthermore, leveraging the dynamic phase control characteristics of liquid crystals in conjunction with metasurfaces presents a viable approach for realizing achromatic and zoom functionalities[30].

According to the principle of phase compensation, most achromatic theories propose a correspondence between a specific parameter and the focalization of light at a particular wavelength. Consequently, focusing light beams of three different wavelengths requires stacking three-layer structures or employing a single-layer lens with three distinct regions for reuse or a unit with three different structural sizes[28,29,31,32]. Recently, this one-to-one relationship has been broken by a metalens doublet in the ref. 33, this double-layer structure achieved RGB achromatism with the high numerical aperture and the polarization-independent property. In order to ensure that the third coupled phase distribution can also match a commonly used wavelength, the structural parameters of stacked meta-atoms were optimized and the reasonable phase deviations were selected. We found that the cascade liquid crystal (LC) Pancharatnam-Berry lens (CLCPBL) could also break the one-to-one relationship without the additional selection and optimization process. The PB phases are generated by the azimuthal angles of liquid crystal molecules, while the coupled PB phases are generated directly by the subtraction between azimuths of different liquid crystal layers. Therefore, for a dual-layer CLCPBL, the three-wavelength achromatism is easy to achieve, but there is no guarantee that these wavelengths are all in the visible range. Once the number of cascade PB lens layers comes to three, three inherent phase distributions and the coupled PB phase distributions generated from the pairwise or triple combination between the three PB lenses can ensure that the number of confocal wavelengths increases to $C_3^1 + C_3^2 + C_3^3 = 7$ and can ensure that these wavelengths are common laser wavelengths. The achromatism can be achieved not only in RGB range, but also in near-infrared and mid-infrared range. Furthermore, the amplitude coefficients of the PB phase terms depend on the phase retardation, which can be flexibly regulated by the voltage applied to the liquid crystal molecules. This implies that the focal intensity of incident light beams of different wavelengths can be adjusted and selected by manipulating the voltage applied to different layers of the cascade lens. The CLCPBL can work with a richer variety of wavelengths and a wider range of wavelengths distribution, and can has a more convenient design and fabrication process.

We theoretically predicted the existence of the coupled PB phase, and proved the three-wavelength achromatic function based on a dual-layer CLCPBL in simulations. Then we fabricated a three-layer CLCPBL with a radius of 3 mm, focal length of 320 mm, and designed wavelengths of 1064, 396.8, and 1550 nm by using single-step photoalignment technology[34]. The feasibility of the multiwavelength achromatic function of the coupled PB phase was proved by light incidence at 1064, 632.8, and 532.8 nm wavelengths, and the function of adjusting the focus intensity based on the voltage was proved by light incidence at 405 nm. The achromatic experimental results were in complete agreement with the simulation results.

Results

Simulation

The liquid crystal is a type of birefringent crystal, and its phase retardation δ can be expressed as $\delta = 2\pi\Delta n_{\text{eff}} d/\lambda_0$, where Δn_{eff} is the effective birefringence index of liquid crystal and can be modulated by applying different voltages, d is the thickness of liquid crystal cell, and λ_0 corresponds to the wavelength of incident light. The angle between the projection of the long axis of the liquid crystal molecule on the xy plane and the x-axis is defined as the azimuth angle θ, and can be controlled by photoalignment to realize different PB phases. Linearly polarized (LP) light passing through the liquid crystal unit was calculated using the Jones matrix. First, for a single-layer liquid crystal, assuming that the LP light input $\begin{bmatrix} E_x \\ E_y \end{bmatrix} = \begin{bmatrix} 0 \\ 1 \end{bmatrix}$ with polarization components Ex and Ey in the x and y directions are incident, the outgoing light matrix $\begin{bmatrix} E_{xout} \\ E_{yout} \end{bmatrix}$ after passing through the liquid crystal layer satisfies the following equation[35–37]

$$\begin{bmatrix} E_{xout} \\ E_{yout} \end{bmatrix} = R(-\theta)T(\delta)R(\theta)\begin{bmatrix} 0 \\ 1 \end{bmatrix} \tag{1}$$

Here, $R(\theta) = \begin{bmatrix} \cos\theta & \sin\theta \\ -\sin\theta & \cos\theta \end{bmatrix}$ is the rotation matrix, and $T = \begin{bmatrix} e^{-\frac{\delta}{2}} & 0 \\ 0 & e^{\frac{\delta}{2}} \end{bmatrix}$ represents the phase retardation generated along the fast axis and the slow axis.

We employed a cascaded configuration of two liquid crystal PB lenses, as shown in Fig. 1a. Each PB lens consisted of two symmetrical glass substrates coated with indium tin oxide (ITO) films and aligning layers, with a nematic liquid crystal infused between the aligning layers. When achieving unit-to-unit alignment for two layers, as illustrated in Fig. 1b, we have PB lens 1 with a phase retardation δ and rotation angle θ, and PB lens 2 with a phase retardation δ' and rotation angle θ'. By applying distinct alternating current (AC) voltages, the phase retardations of the two PB lenses can also be modified, which corresponds to the alteration in the angle between the liquid crystal molecule director (indicated by the red arrow) and the z-axis in Fig. 1b.

The beam passes through units of two layers and finally exits, which is equivalent to applying the Jones matrix transformation twice and can be written as

$$\begin{bmatrix} E_{xout} \\ E_{yout} \end{bmatrix} = R(-\theta')T(\delta')R(\theta')R(-\theta)T(\delta)R(\theta)\begin{bmatrix} 0 \\ 1 \end{bmatrix} \tag{2}$$

Decomposing the result as left circularly polarized (LCP) light E_L and right circularly polarized (RCP) light E_R, respectively, we get

$$E_L = \frac{1}{2}\left\{\sin\frac{\delta}{2}\cos\frac{\delta'}{2}e^{-i2\theta} - i\cos\frac{\delta}{2}\cos\frac{\delta'}{2} + i\sin\frac{\delta'}{2}\sin\frac{\delta}{2}e^{i2(\theta-\theta')} + \sin\frac{\delta'}{2}\cos\frac{\delta}{2}e^{-i2\theta'}\right\}\begin{bmatrix} 1 \\ i \end{bmatrix} \tag{3}$$

$$E_R = -\frac{1}{2}\left\{\sin\frac{\delta}{2}\cos\frac{\delta'}{2}e^{i2\theta} - i\cos\frac{\delta}{2}\cos\frac{\delta'}{2} + i\sin\frac{\delta'}{2}\sin\frac{\delta}{2}e^{-i2(\theta-\theta')} + \sin\frac{\delta'}{2}\cos\frac{\delta}{2}e^{i2\theta'}\right\}\begin{bmatrix} 1 \\ -i \end{bmatrix} \tag{4}$$

The given Eqs. (3) and (4) include three PB phase components, namely $\pm\theta$, $\pm\theta'$, and $\pm\theta - \theta'$, which can be associated with the phases of the three wavelengths λ_0, λ_1, and λ_2, respectively. Hence, after the plane wave is incident, the azimuthal rotation angles θ at different positions on PB lens 1 will cause that the PB phases meet the phase shift of the gradient, such that the wavefront converges of λ_0 to a focal point, the formula is as follows[27]

$$\theta(x, y, \lambda_0) = \frac{\pi}{\lambda_0}\left(\sqrt{x^2 + y^2 + f^2} - f\right) \tag{5}$$

where x and y are the position coordinates of the unit in the plane, and f is the focal length of the PB lens set. In order to have a phase gradient at the same position (x, y) on another plane of PB lens 2 for light of varying wavelengths, we can obtain

$$\theta'(x, y, \lambda_1) = \frac{\pi}{\lambda_1}\left(\sqrt{x^2 + y^2 + f^2} - f\right) = \frac{\lambda_0}{\lambda_1}\theta(x, y, \lambda_0) \tag{6}$$

$$\theta - \theta' = \left(\frac{1}{\lambda_0} - \frac{1}{\lambda_1}\right)\lambda_0\theta(x, y, \lambda_0) = \frac{1}{\lambda_2}\lambda_0\theta(x, y, \lambda_0) \tag{7}$$

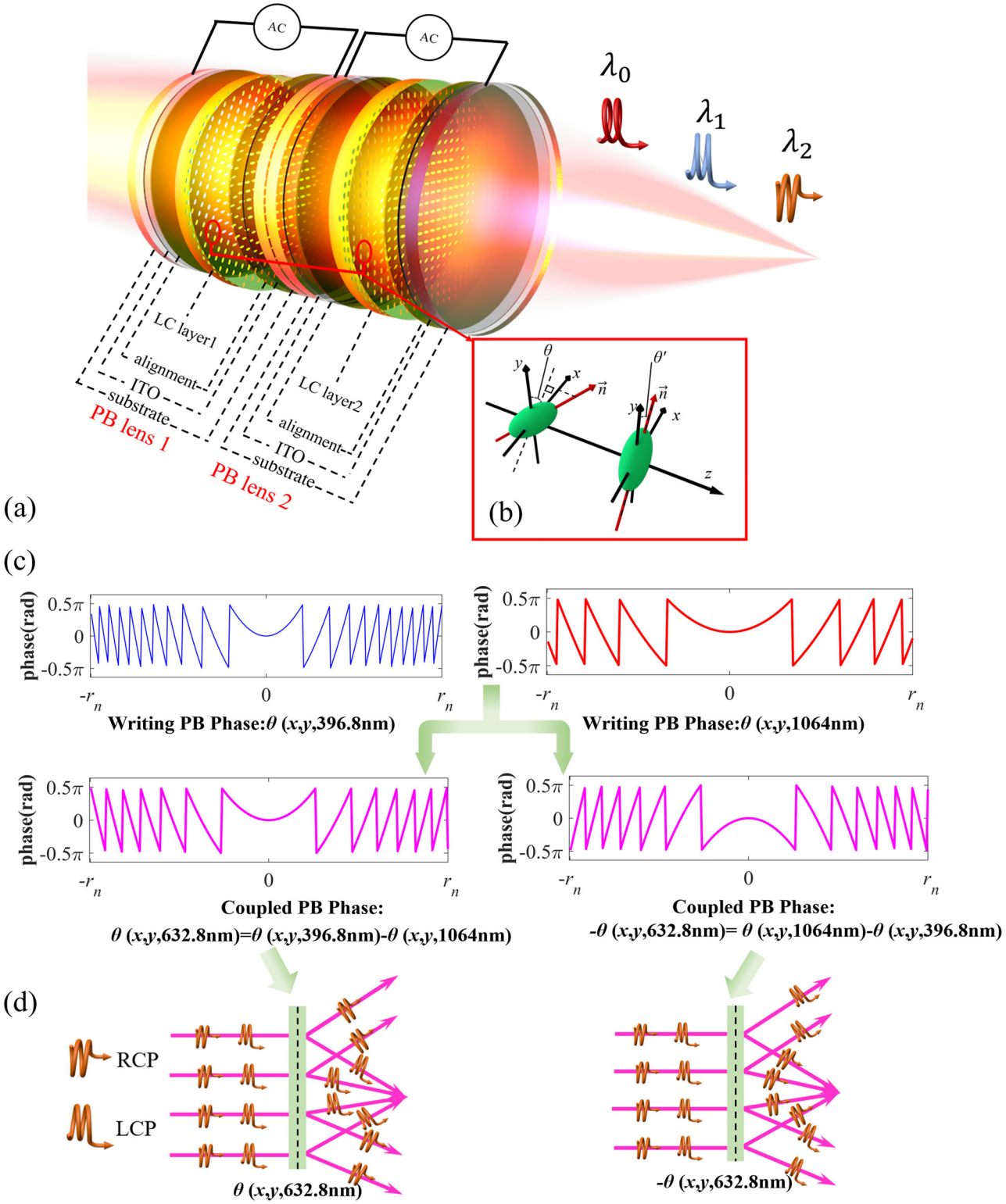

Fig. 1 | Schematic of a dual-layer cascade liquid crystal Pancharatnam-Berry lens. **a** Schematic of two cascaded Pancharatnam-Berry (PB) lenses to achieve three-wavelength achromatic function. A cell is formed by two face-to-face "alignment-indium tin oxide (ITO) - substrate" structures, and a liquid crystal (LC) layer is injected into the cell to form a single PB lens. The other PB lens has the same structure, except that the liquid crystal layer is different. Alternating current (AC) voltage is applied to each PB lens to change the focus intensity. **b** Diagram of the arrangement states of two liquid crystal molecules for pixel-to-pixel alignment. The two liquid crystal molecules have different pointing vectors (red arrows), which lead the different rotation angles in two *x*-*y* planes. **c** The phase profiles of PB lenses with designed wavelengths 396.8 and 1064 nm will form a coupled phase profile for target wavelengths 632.8 nm. Switching the sequence order of coupling between wavelengths 396.8 and 1064 nm will result in a pair of coupled phases of opposite concave-convex characteristics. **d** Schematic of the polarizations of the foci formed by a pair of opposite chiral plane waves incident on different PB lenses with opposite phase profile.

Therefore, two layers of PB lenses are designed first, the radius and the focal length of both lenses are set to 15.1 and 25 μm, respectively, and the characteristic size of each phase unit is 100 nm, the designed wavelengths for two lenses are set to 1064 and 396.8 nm. By setting $\lambda_0 = 396.8\text{nm}$ and $\lambda_1 = 1064\,\text{nm}$, the writing phase profiles of rotation angles are shown in Fig. 1c, respectively, which would generate a coupled PB phase term $\theta - \theta' = \theta(x, y, 398.8\text{nm}) - \theta'(x, y, 1064\text{nm}) = \theta(x, y, 632.8\text{nm})$. Similarly, by setting $\lambda_0 = 1064\text{nm}$ and $\lambda_1 = 396.8\text{nm}$ would generate a coupled PB phase term $\theta - \theta' = \theta(x, y, 1064\text{nm}) - \theta'(x, y, 396.8\text{nm}) = -\theta(x, y, 632.8\text{nm})$. Both settings focus light of three wavelengths; however, the chiralities of the polarization state of the focal point with a wavelength of 632.8 nm are opposite, as shown in Fig. 2d. In summary, when the wavelength λ_2 satisfies the $|\theta - \theta'| = \left|\frac{1}{\lambda_0} \pm \frac{1}{\lambda_1}\right|\lambda_0\left(\sqrt{x^2 + y^2 + f^2} - f\right)$, all three wavelengths can be confocal, but the chirality of the light at the focal point may be different. Here, we have derived the case of incident LP light which focuses on one kind of chiral light and then diverges from the opposite chiral light. Therefore, when we choose the appropriate chiral incident light, there would be no divergence.

The wavelength range is limited because ultraviolet light causes damage to liquid crystal molecules. And the modulation of long wavelengths requires a large amount of phase retardation, leading to a large increase in the thickness of the liquid crystal layer which causes significant problems in the process. However, through further research on inorganic liquid crystals[38] and terahertz liquid crystals[39], the wavelength range may be extended to a wider range, from ultraviolet to far-infrared.

According to the aforementioned parameters, we performed Finite-difference time-domain (FDTD) simulation and selected three incident wavelengths λ_0 (1064 nm), λ_1 (396.8 nm), and λ_2 (632.8 nm). As shown in Fig. 2a, we set the thickness d of the bottom layer (Layer2) as 3.0175 μm and the liquid crystal molecular rotation angle θ according to the formula $\theta(x, y, 1064\,\text{nm})$ for distribution, indicating the designed wavelength is 1064 nm; similarly, the thickness d' of the top layer(Layer1) is 2.48 μm and the liquid crystal molecular rotation angle θ' is set according to the formula $\theta\prime(x, y, 396.8\,\text{nm})$ for distribution; furthermore, the designed wavelength is 396.8 nm. Additionally, according to the coupled PB phase theory, incident light with a wavelength of 632.8 nm is focused at the same focal point. Ordinary optical refractive index n_o of the dual-layer liquid crystal lens is set to 1.5, extraordinary optical refractive index n_e can be artificially changed, and the effective birefringence are denoted to $\Delta n'_{\text{eff}}$ and Δn_{eff}, respectively, which means that the amplitude coefficient before each phase term can be changed. The specific design parameters are listed in Table 1. Six sets of simulations with different parameters were set in total, which correspond to the simulation results in b, c, d, f, i, j, and g in Fig. 2.

When the LP plane waves with wavelengths of 1064, 632.8, and 396.8 nm are applied to be incident on the structure, each effective refractive index is adjusted to maximize the amplitude coefficient at this wavelength. The focusing results are shown in Fig. 2b–d. The plane wave emerges from the dual-layer PB lens at z = 0 μm and is confocal at the transmission distance of approximately 22 μm, which differs from the designed focal length of 25 μm. This is because the refractive index of the liquid crystal layer is larger than that of air, and the thickness of the liquid crystal layer results in an equivalent optical path.

Subsequently, as shown in the right image of Fig. 2e, by varying the effective refractive index, the amplitude coefficients before each phase term are equal. A dual-layer PB lens is equivalent to three PB lenses with designed wavelength of 396.8, 632.8, and 1064 nm, which can form the three-focus phenomenon with a beam of 1064 nm wavelength irradiation. Due to the negative dispersion characteristic of the diffraction lens, the three focal points are arranged from nearest to farthest, and the farthest focal point is located at $f = 22$ μm. The simulation results in Fig. 2f verify this phenomenon, which also prove that the focal intensity is adjustable and assignable. The left image of Fig. 2e shows that when the above layer of liquid crystal rotation angle distribution is set to $-\theta'(x, y, 396.8\,\text{nm})$, the coupled PB phase will change, theoretically form a lens with designed wavelength as 296 nm and focal point at $f = 22$ μm. Hence, for 1064 nm wavelength incidence, the focal distance formed by the coupled phase distributions generated as $\theta(x, y, 1064\,\text{nm}) - \theta'(x, y, 396.8\,\text{nm})$ is larger than formed by the coupled phase distributions generated as $\theta(x, y, 1064\,\text{nm}) + \theta\prime(x, y, 396.8\,\text{nm})$. Figure 2g proves this phenomenon; however, because of the close location of the focus, the two focal points are difficult to distinguish. Additionally, Fig. 2f and g shows that if the designed wavelength (396.8 nm or 296 nm) of the PB lens is different from the incident wavelength (1064 nm), the focus intensity will be weaker because the phase mismatch results in only part of the phase moderating the incident light to form a focus, whereas other phases will cause random disturbance of the incident light.

Finally, as shown in Fig. 2h, the dual-layer PB lens is controlled by phase retardation such that it is equivalent to the single-layer PB lens with a designed wavelength of 1064 nm. When the beams with wavelengths of 396.8 nm and 632.8 nm incident this structure, it would theoretically form negative dispersion and the focal position would be far from the preset focal length. As shown in Fig. 2i and j, foci could not be formed in the simulation area, and the simulation verified the expected results.

Therefore, it is proven that the coupled PB phase between the dual-layer PB lens is formed, and the focusing of a specific wavelength of light can be achieved.

Experiment

Furthermore, we extended the double-layer structure to a three-layer CLCPBL. Therefore, there were three separate writing PB phase gradients, three pairwise coupled PB phases, and one PB phase obtained by coupling the three layers together. Theoretically, seven different wavelengths can be considered as confocal wavelengths. As shown in Table 2, there is a correlation between the phase distributions of seven different wavelengths. Metalenses generally require subwavelength-scale units to obtain a phase gradient, which also means that cascading metalenses require high-precision displacement for processing and pixel alignment. This is achievable in engineering, but it is not necessary. In order to simply verify the existence of the coupled PB phase and these PB phases can achieve multi-wavelength achromatic aberrations, we used a single-step exposure optical path[34] for PB phase writing, and finally prepared a three-layer CLCPBL with an area of 6 mm × 6 mm and phase units of 8 μm × 8 μm.

Figure 3a shows the phase profiles of these PB lenses, where the combination of three layers of PB lenses with writing PB phases at 1064, 396.8, and 1550 nm yield rich coupled phases at 3383.5, 632.8, 450, and 532.8 nm. It can be seen that the shorter the design wavelength, the narrower the outer ring width of the PB lens, which causes a lower diffraction efficiency because of the finite number of phase levels. This also indicates that even when the coupled PB phase can form multiwavelength focusing, the focusing effect of different wavelengths differs when the lens diameter is limited. Figure 3b illustrates the phase gradients at the edges of several lenses shown in Fig. 3a. Among them, the phase gradient of the outermost ring of the PB lens with the shortest design wavelength of 396.8 nm has five levels, that of the outermost ring of the PB lens with a design wavelength of 1064 nm has six levels, and that of the outermost ring of the PB lens with a design wavelength of 632 nm has six levels. According to diffraction theory[40], the diffraction efficiency of the five levels grating is approximately 87.5%, which implies that the overall diffraction efficiency of the PB lens is sufficiently high under these phase distributions. Figure 3c, d shows photographs of the CLCPBL with and without orthogonal polarizers, respectively. Figure 3e–g shows the discrete individual PB Lenses. The oriented regions are enclosed within the red boxes, whereas the outer regions exhibit a disordered liquid crystal distribution. Additionally, irregularly colored fringes were observed owing to the nonuniform cell thickness.

The focusing results were tested, as shown in Fig. 4a, the CLCPBL was fixed to a section of the optical guide rail and the beam profiler was moved along the guide rail to observe the focusing effect at different wavelengths.

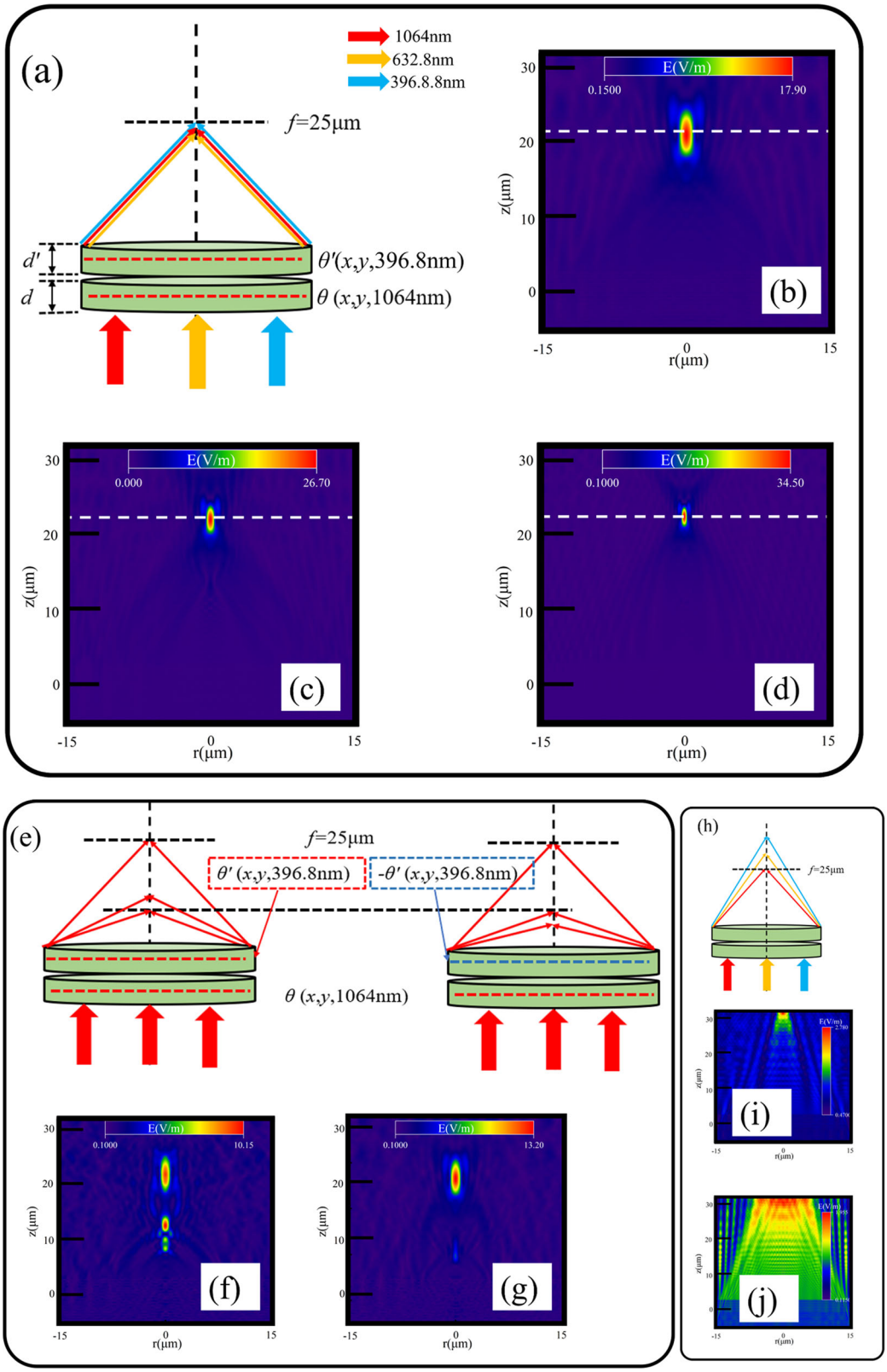

Fig. 2 | Simulation result. a The focusing situation of linearly polarized plane waves with three different wavelengths (1064 nm, 632.8 nm, 396.8 nm) incident on the dual-layer CLCPBL. **b–d** represent the simulation results respectively of 1064 nm, 632 nm and 396.8 nm incident under the maximum amplitude coefficient. The white dashed line represents the focal plane. **e** represents the modulation effect of PB phase and coupled PB phase on the incident monochromatic wave, resulting multiple focal points. Different coupled PB phases will lead to differences in the position of the focal points. **f**, **g** represent the simulation results showing the positions of multiple focal points. **h** indicates that the modulation phase retardation causes the upper PB lens to become ineffective. When a plane wave with the wavelength of 632.8 nm or 396.8 nm is incident on the PB lens with a designed wavelength of 1064 nm, it will exhibit negative dispersion. **i**, **j** show the simulation results of negative dispersion for the beams with wavelengths of 632.8 nm and 396.8 nm, respectively.

Table 1 | Simulation parameters of dual-layer liquid crystal Pancharatnam-Berry lens

Layer1(d' = 2.48 μm) : θ' (x, y, 396.8 nm); Layer2(d = 3.018 μm) : θ (x, y, 1064 nm)							**Layer1(d' = 2.48 μm): $-\theta'$ (x, y, 396.8 nm); Layer2(d = 3.018 μm): θ (x, y, 1064 nm)**
Incident wavelength (nm)	1064	396.8	632.8	1064	632.8	396.8	1064
$\Delta n'_{eff}$	0	0.24	0.1275	0.107	0	0	0.107
Δn_{eff}	0.1763	0	0.1047	0.088	0.1763	0.1763	0.088
$\sin\frac{\delta'}{2}\cos\frac{\delta}{2}$	0	1	0	0.49	0	0	0.49
$\sin\frac{\delta'}{2}\sin\frac{\delta}{2}$	0	0	1	0.49	0	0	0.49
$\sin\frac{\delta}{2}\cos\frac{\delta'}{2}$	1	0	0	0.49	0.48	0.8773	0.49
Fig. 2 results	b	c	d	f	i	j	g

Table 2 | Phase distribution of different Pancharatnam-Berry lenses

Lens	Designed wavelength(nm)	PB phase
1[a]	1064	θ_1
2[a]	396.8	$\theta_2 = 2.681\theta_1$
3[a]	1550	$\theta_3 = 0.686\theta_1$
4[b]	3383.5	$\theta_4 = \theta_1\text{-}\theta_3 = 0.314\theta_1$
5[b]	632.8	$\theta_5 = \theta_1\text{-}\theta_2 = -1.681\theta_1$
6[b]	532.8	$\theta_6 = \theta_2\text{-}\theta_3 = 1.995\theta_1$
7[b]	450	$\theta_7 = \theta_1\text{-}\theta_2\text{-}\theta_3 = -2.367\theta_1$

[a]Writing PB phase.
[b]Coupled PB phase.

Figure 4b illustrates the focusing of a 632.8 nm wavelength beam incident on a single-layer PB lens with a designed wavelength of 632.8 nm and a focal length of 320 mm. It can be observed that as the beam profiler moves along the rail, defining the distance from the PB lens as z, a focused spot is formed at approximately z = 320 mm, demonstrating that the functionality of our fabricated single-layer PB lens meets the expectations. Figure 4c shows the focusing of beams with different wavelengths incident on the fabricated three-layer CLCPBL. In this case, all the three wavelengths formed a focus of approximately 320 mm. The PB lens designed for a designed wavelength of 1064 nm is experimentally fabricated, while the focusing of the beams at wavelengths of 632.8 and 532.8 nm is achieved through the coupled PB phase, thus verifying the chromatic aberration correction functionality. Figure 4d demonstrates the multi-focus phenomenon when a 632.8 nm beam is incident on the cascaded lens. Owing to the high brightness and nonadjustability of the laser, a small aperture was used to select a portion of the beam for incidence, resulting in two prominent side lobes on either side of the focal spot. However, this did not affect our results. Figure 4e shows the focal spot formed at z = 320 mm when a 532.8 nm laser diode is incident on the cascaded PB lens, while Fig. 4f shows the variation in focal spot intensity by adjusting the applied voltage at both ends of the PB lens with a designed wavelength of 396.8 nm when a 405 nm laser is incident on the cascaded PB lens. It can be observed that as the phase retardation decreases, the focal spot intensity eventually reaches zero.

Discussion

We must point out that the simulation result is under an ideal condition (a very small pixel size and neglecting the glass thickness), so the CLPBL in the simulation can have a high numerical aperture. This simulation is only to verify that the coupled PB phases are effective, and does not mean that the actual prepared CLPBL in the experiment can have such a high numerical aperture. In fact, it is less feasible to satisfy these ideal conditions in the actual fabrication process, and our experimental conditions are not sufficient. Therefore, this design scheme with the larger pixel size and the thicker glass thickness can only be applied to the preparation of the CLPBL under a small numerical aperture at present. For the effects of the pixel size and the glass thickness on the numerical aperture can be found in Supplementary Note 1.

This set of wavelength relations of our design exactly satisfies the achromatic aberration of several common laser wavelengths. However, choosing other intrinsic wavelength parameters cannot guarantee that the coupled wavelength is the commonly used, such as in a two-layer cascade structure, the third wavelength (842 nm) is determined by the two intrinsic wavelengths (405 nm and 780 nm). Obviously, the third wavelength is not commonly used according to the matching result, and thus this design solution will lack degrees of freedom in some application scenarios. So, our work may be different from some other works, for example, the ref. 33 allows the free choice of the design wavelength. To be honest, the low numerical aperture and the determined wavelengths selection are also unavoidable drawbacks of our work.

Here we will give a specific explanation of the causes of the bad focal spot performance in Fig. 4c. Firstly, the 532 nm laser was emitted by a laser diode, whose beam quality was not very good, and the phase accuracy during processing was not high enough which affect the coupled phases directly. Another main reason might come from the alignment problem because the focal spot was not located at the center of the background ring band in Fig. 4c. The misalignment between the layers would cause the phase distributions of 532.5 nm no longer has rotational symmetry property, so the focal spot morphology and intensity distribution would change accordingly. The errors mentioned above will also lead to the reduction of the diffraction efficiency, and a more detailed analysis can be found in the Supplementary Note 2. For the three wavelengths of 1064, 532.8 and 632.8 nm, the theoretical diffraction efficiencies are 64.65%, 64.16% and 63.94%, respectively, whereas the actual diffraction efficiencies of our test are 41.4%, 32.1% and 37.3%.

As the process can be further optimized, the number of layers of the cascade can be further increased, for example, 6 layers can theoretically bring 63 focus points, or 63 wavelengths of achromatic aberration which are expected to be applied to rich scenarios such as laser cutting, 3D imaging and VR/AR. The design of the coupled PB phase can also be applied in optical information encryption, optical communication and optical detection[41,42].

In summary, this cascade liquid crystal PB phase lens utilizes the coupled PB phase caused by the rotation angle difference to achieve multiwavelength focusing. The coupled PB phase is proportional to the difference of optical frequencies. This basic principle coincides with the band width of laser material and enables this cascaded structure to satisfy the commonly used range of wavelengths.

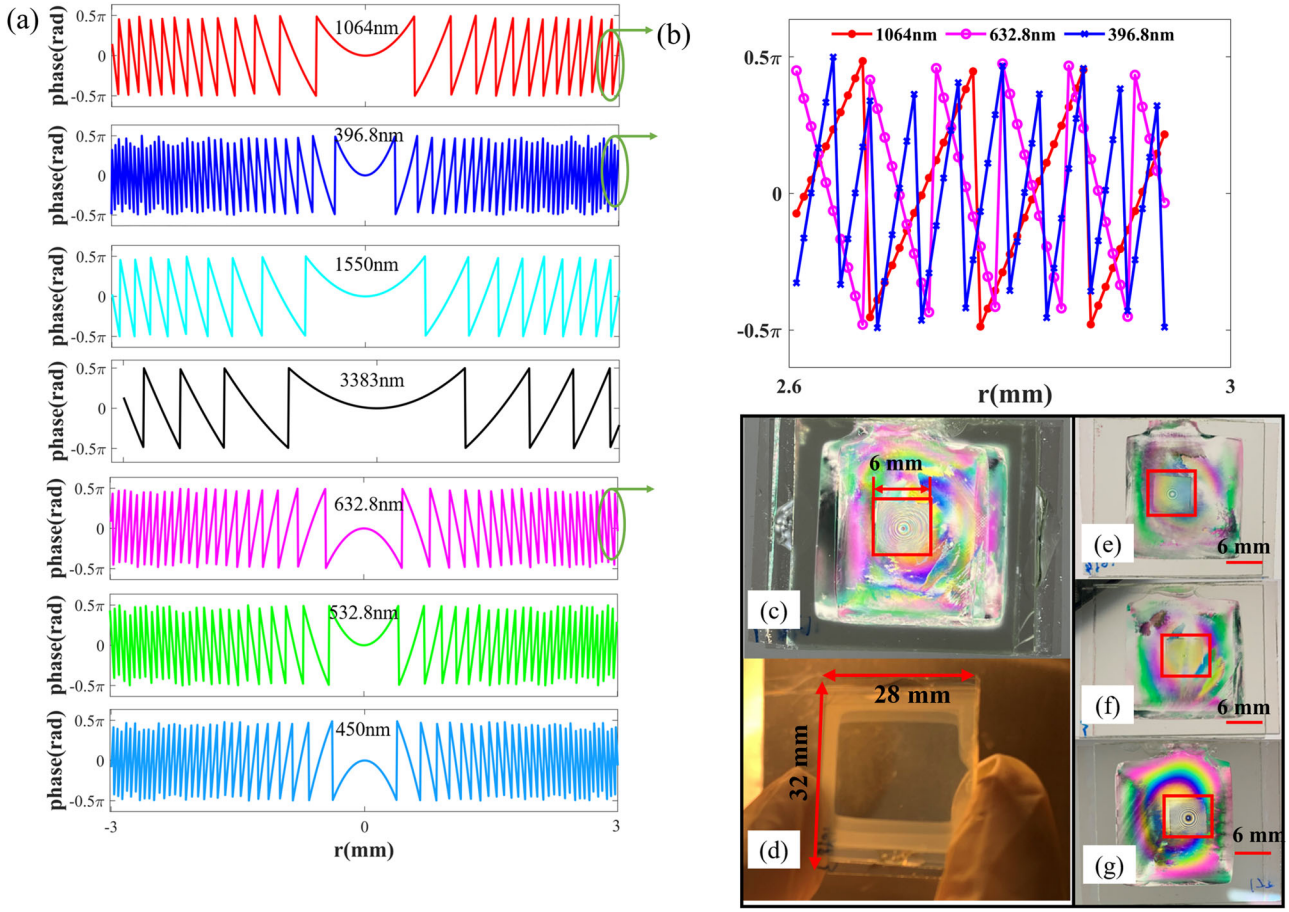

Fig. 3 | Pancharatnam-Berry phase distribution diagram. a The profile of writing PB phases and coupled PB phases. **b** The phase gradient levels at the edge of the PB lenses for the designed wavelengths of 396.8, 632.8, and 1064 nm. For 396.8, 632.8, and 1064 nm wavelengths, the phase curves for the three wavelengths are denoted by red line, pink line, and blue line, respectively; and their phase gradients are denoted by red solid circles, pink hollow circles, and blue saltires, respectively. **c**, **d** Photographs of the cascaded liquid crystal PB lenses under orthogonal polarizers and without polarizers, respectively. **e**–**g** Represent individual liquid crystal PB lenses for the designed wavelengths of 1064, 396.8, and 1550 nm, respectively, both red frame sizes are 6 mm × 6 mm.

This design idea of the coupled PB phase is still suitable for the cascading of other metalenses based on the PB phase. This simple design, combined with the easy processing and adjustable characteristics of liquid crystals, provides a solution for optical systems that are compact, lightweight, and have multi-scenario applications.

Methods

Preparation of CLCPBL

The wavelength of the exposure light source is 405 nm (CNIlaser, China), and the pixel size of the spatial light modulator (SLM) is 8 μm × 8 μm (Holoeye, Germany). Under a 1:1 imaging condition, the pixel scale of the PB phase was also 8 μm × 8 μm. This large-scale phase arrangement indicates that the smooth phase gradient becomes a multi-level phase gradient; however, this is still valid for multiwavelength confocal systems. The scale of the phase unit can also be reduced by means of microimaging and displacement stage splicing, which can smooth the phase gradient and obtain a higher diffraction efficiency.

The fabrication process for the three-layer cascaded PB lens is illustrated in Fig. 5a. A layer of a photoalignment film (Lia-s, DIC, Japan) was spin-coated onto two pieces of ITO glass. Subsequently, frame glue was applied to one of the alignment layers and the two alignment layers were pressed together to create empty cells in the gap. The exposure light path illustrated in Fig. 5b was utilized for photoalignment, which took only a few minutes to complete. Specifically, the laser passes through a beam expander and a polarizer and is then imaged onto the surface of an SLM device using a lithographic-grade aperture (6 mm × 6 mm), which controls the phase retardation by loading grayscale images. The modulated beam passes through a quarter-wave plate and is imaged onto the sample surface. The laser polarization direction, SLM orientation, and rotation angle of the quarter-wave plate satisfied specific relationships, resulting in the formation of oriented light patterns in the photoalignment layer. Subsequently, liquid crystal (Hecheng Display, China) is injected into the cell and the box is sealed with curing glue, resulting in a single-layer lens with an area of 6 mm × 6 mm and phase units of 8 μm × 8 μm. Following the same procedure, another empty cell was exposed, and liquid crystals were injected again, followed by the sealing of the cell to obtain a double-layer lens. A three-layer CLCPBL is fabricated by repeating this process.

Equipments for testing optical path

Four different lasers were used in the focusing experiment: a 405 nm semiconductor laser (CNIlaser, China), 532.8 nm laser diode (Thorlabs, America), 632 nm continuous laser and 1064 nm pulsed laser (SIOM, China).

Reporting summary

Further information on research design is available in the Nature Portfolio Reporting Summary linked to this article.

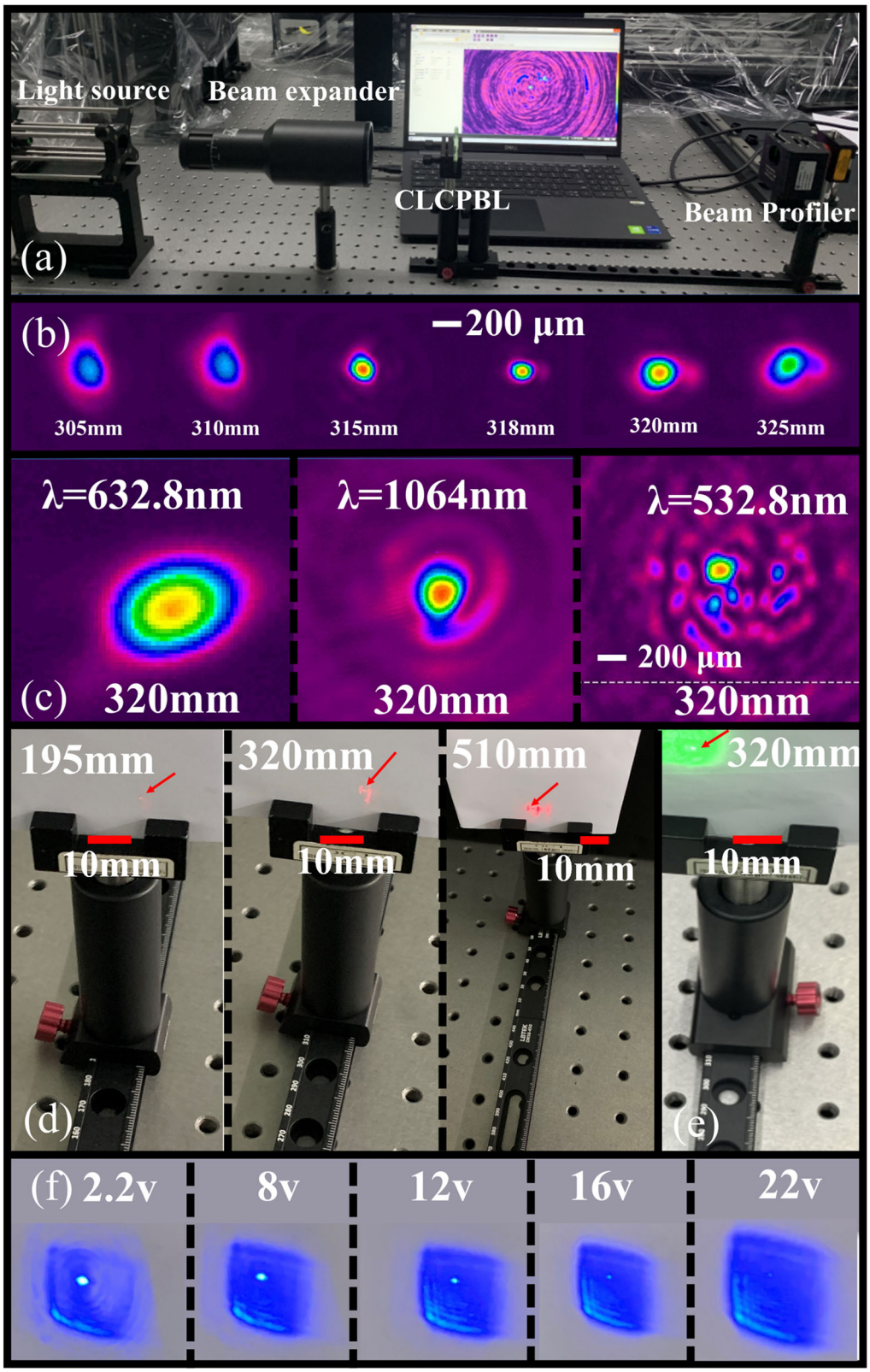

Fig. 4 | Experimental results on focusing. a Focusing assessment system. **b** Beam spot patterns acquired at various distances when a laser with a wavelength of 632.8 nm is incident on a single-layer Pancharatnam-Berry lens for a designed wavelength of 632.8 nm and a focal length of 320 mm. **c** Beam profile patterns at the designed focal position for incident beams with wavelengths of 1064, 632.8, and 532.8 nm after passing through a three-layer cascade liquid crystal Pancharatnam-Berry lens (CLCPBL). **d** Photographs of multiple focal points generated by 632 nm light at different positions after passing through a three-layer CLCPBL. **e** Photograph of focused spot at the focal point with 532 nm light. **f** Photograph depicting the variation in focal intensity of a 405 nm laser incident on the CLCPBL as the voltage is modulated.

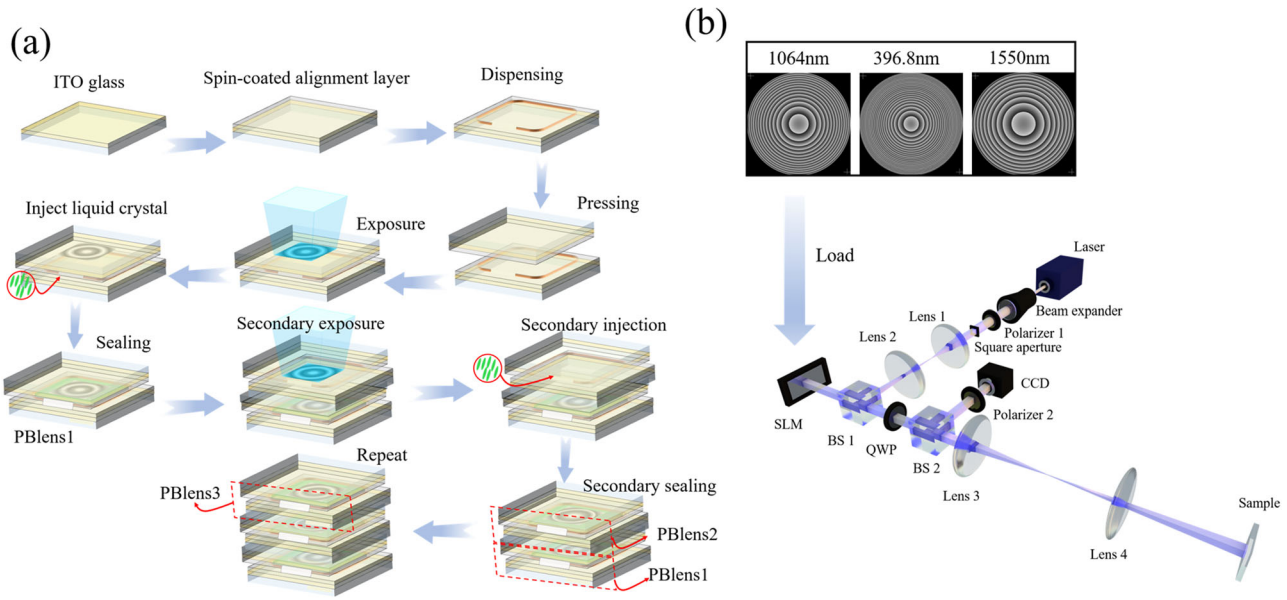

Fig. 5 | Process flowchart of cascade liquid crystal Pancharatnam-Berry lens fabrication. a For the single Pancharatnam-Berry lens fabrication, photoalignment films are spin-coated on two pieces of ITO glass, and framing adhesive is applied to the photoalignment film of one of the pieces. The photoalignment film surfaces on the two pieces of glass are then aligned and pressed together to form a cavity. A laser is used to expose the photoalignment layer. Finally, liquid crystals are injected and the cavity is completely sealed. The remaining PB lenses follow this procedure, except that the exposure must be aligned with the first exposure. **b** Photoalignment exposure path. After the greyscale pattern is loaded into the spatial light modulator (SLM), the laser passes through a beam expander and a polarizer, then irradiates the square aperture, the light field is imaged onto the SLM via lens 1 and lens 2. The image field is modulated by the SLM and quarter wave plate (QWP), and then imaged onto the surface of the sample again by lens 3 and 4. The charge coupled device (CCD) receives the reflected light from the sample to observe the exposure process, two beam splitting (BS) prisms are used to change the direction of the light path.

Data availability

All the data presented in the manuscript are available upon a reasonable request to the corresponding author.

Code availability

Codes used in the analysis of the results are available upon a reasonable request to the corresponding author.

Received: 13 September 2023; Accepted: 18 March 2024;
Published online: 01 April 2024

References

1. Wang, Y. et al. High-efficiency broadband achromatic metalens for near-IR biological imaging window. *Nat. Commun.* **12**, 5560 (2021).
2. Cai, T. et al. Ultrawideband chromatic aberration-free meta-mirrors. *Adv. Photon.* **3**, 016001 (2020).
3. Richards, C. A. et al. Hybrid achromatic microlenses with high numerical apertures and focusing efficiencies across the visible. *Nat. Commun.* **14**, 3119 (2023).
4. Born, M., Wolf, E. *Principles of optics: electromagnetic theory of propagation, interference and diffraction of light. Ch. 4*. (Cambridge University Press & Publishing House of Electronics Industry, 2016).
5. Farn, M. W. et al. Color separation by use of binary optics. *Opt. Lett.* **18**, 1214–1216 (1993).
6. Kipp, L. et al. Sharper images by focusing soft X-rays with photon sieves. *Nature* **414**, 184–188 (2001).
7. Cao, Q. & Jahns, J. Nonparaxial model for the focusing of high-numerical-aperture photon sieves. *J. Opt. Soc. Am. A* **20**, 1005–1012 (2003).
8. Harm, W. et al. Dispersion tuning with a varifocal diffractive-refractive hybrid lens. *Opt. Expr.* **22**, 5260–5269 (2014).
9. Stone, T. & George, N. Hybrid diffractive-refractive lenses and achromats. *Appl. Opt.* **27**, 2960–2971 (1988).
10. Sanli, U. T. et al. Apochromatic X-ray focusing. *Light: Sci. Appl.* **12**, 107 (2023).
11. Li, Y. et al. Broadband cholesteric liquid crystal lens for chromatic aberration correction in catadioptric virtual reality optics. *Opt. Expr.* **29**, 6011–6020 (2021).
12. Lin, D. et al. Dielectric gradient metasurface optical elements. *Science* **345**, 298–302 (2014).
13. Wen, D. et al. Light field on a chip: metasurface-based multicolor holograms. *Adv. Photon.* **3**, 024001 (2021).
14. Khorasaninejad, M. et al. Metalenses at visible wavelengths: Diffraction-limited focusing and subwavelength resolution imaging. *Science* **352**, 1190–1194 (2016).
15. Li, G., Zhang, S. & Zentgraf, T. Nonlinear photonic metasurfaces. *Nat. Rev. Mater.* **2**, 17010 (2017).
16. Ni, X., Kildishev, A. V. & Shalaev, V. M. Metasurface holograms for visible light. *Nat. Commun.* **4**, 2807 (2013).
17. Kim, J. et al. Tunable metasurfaces towards versatile metalenses and metaholograms: a review. *Adv. Photon.* **4**, 024001 (2022).
18. Deng, Z. et al. Vectorial compound metapixels for arbitrary nonorthogonal polarization steganography. *Adv. Mater.* **33**, 2103472 (2021).
19. Luo, Y. et al. Varifocal metalens for optical sectioning fluorescence microscopy. *Nano. Lett.* **21**, 5133–5142 (2021).
20. Luo, X. Plasmonic metalens for nanofabrication. *Natl Sci. Rev.* **5**, 137–138 (2018).
21. Pan, M. et al. Dielectric metalens for miniaturized imaging systems: progress and challenges. *Light: Sci. Appl.* **11**, 195 (2022).
22. Lee, G. Y. et al. Metasurface eyepiece for augmented reality. *Nat. Commun.* **9**, 4562 (2018).
23. Hayward, T. M. et al. Multilevel diffractive lens in the MWIR with extended depth-of-focus and wide field-of-view. *Opt. Expr.* **31**, 15384–15391 (2023).
24. Zhang, K. et al. Generating dual-polarized vortex beam by detour phase: From phase gradient metasurfaces to metagratings. *IEEE Trans. Microw. Theory Tech.* **70**, 200–209 (2021).

25. Xu, Q. et al. Mechanically reprogrammable Pancharatnam–Berry metasurface for microwaves. *Adv. Photon.* **4**, 016002 (2022).
26. Bomzon, Z. et al. Space-variant Pancharatnam-Berry phase optical elements with computer-generated subwavelength gratings. *Opt. Lett.* **27**, 1141–1143 (2002).
27. Aieta, F. et al. achromatic metasurfaces by dispersive phase compensation. *Science* **347**, 1342–1345 (2015).
28. Lin, D. et al. Photonic multitasking interleaved Si nanoantenna phased array. *Nano. Lett.* **16**, 7671 (2016).
29. Avayu, O. et al. Composite functional metasurfaces for multispectral achromatic optics. *Nat. Commun.* **8**, 14992 (2017).
30. Shen, Z. et al. Liquid crystal integrated metalens with tunable chromatic aberration. *Adv. Photon.* **2**, 036002–036002 (2020).
31. Arbabi, E. et al. Two-photon microscopy with a double wavelength metasurface objective lens. *Nano. Lett.* **18**, 4943 (2018).
32. Lin, R. et al. Achromatic metalens array for full-colour light-field imaging. *Nat. Nanotechnol.* **14**, 227–231 (2019).
33. Feng, W. et al. RGB achromatic metalens doublet for digital imaging. *Nano. Lett.* **22**, 3969–3975 (2022).
34. Li, Y. et al. Single-exposure fabrication of tunable Pancharatnam-Berry devices using a dye-doped liquid crystal. *Opt. Expr.* **27**, 9054–9060 (2019).
35. Huang, X. et al. Tiger Amulet inspired high-security holographic encryption via liquid crystals. *Nanophotonics* **12**, 1787–1795 (2023).
36. Padmini, H. N. et al. Azimuthal anchoring strength in photopatterned alignment of a nematic. *Crystals* **11**, 675 (2021).
37. Kim, J. et al. Fabrication of ideal geometric-phase holograms with arbitrary wavefronts. *Optica* **2**, 958–964 (2015).
38. Huang, Z. et al. Advances in magneto-optical birefringence effect of 2D materials with extremely large aspect ratio. *Appl. Phys. Lett.* **121**, 220505 (2022).
39. Fan, F. et al. Spin-decoupled beam steering with active optical chirality based on terahertz liquid crystal chiral metadevice. *Adv. Mater. Interfaces* **10**, 2202103 (2023).
40. Ossiander, M. et al. Extreme ultraviolet metalens by vacuum guiding. *Science* **380**, 59–63 (2023).
41. Shi, T. et al. Planar chiral metasurfaces with maximal and tunable chiroptical response driven by bound states in the continuum. *Nat. Commun.* **13**, 4111 (2022).
42. Devlin, R. C. et al. Arbitrary spin-to–orbital angular momentum conversion of light. *Science* **358**, 896–901 (2017).

Acknowledgements

We thank senior engineer Dawei Li of Shanghai Institute of Optics and Fine Mechanics, Professor Zilan Deng of Jinan University, and Dr. Mengmeng Chai of Taiyuan University of Technology for their support in this work. We acknowledge financial support from National Natural Science Foundation of China (Grant No. 52002271), CAS Special Research Assistant Project, China Postdoctoral Science Foundation (Grant No.2021M703326), Key foreign cooperation projects of Bureau of International Cooperation of Chinese Academy of Sciences (Grant No. 181231KYSB20210001) and Cooperation project with Hong Kong, Macao and Taiwan supported by Science and Technology Commission of Shanghai Municipality (Grant No. 22220760300).

Author contributions

Z.M., Y.-A.Z. and J.W. conceived the project. C.C., Q.C and J.S provided the theoretical guidance. Y.C., Y.-D.Z., S.O., Z.C. improved the process and fabricated the samples. X.Z., Z.Z. measured the sample. X.L., K.W. performed the data processing. All authors have given approval to the final version of the manuscript.

Competing interests

The authors declare no competing interests.

Additional information

Supplementary information The online version contains supplementary material available at https://doi.org/10.1038/s42005-024-01601-0.

Correspondence and requests for materials should be addressed to Yuanan Zhao, Qing Cao or Jianda Shao.

Peer review information *Communications Physics* thanks the anonymous reviewers for their contribution to the peer review of this work. A peer review file is available.